

<https://doi.org/10.1038/s44303-026-00143-0>

Predictive modeling of chronic foot ulcer outcomes using longitudinal photoacoustic imaging

Check for updates

Yanda Cheng¹, Chuqin Huang¹, Shu-liang Yu², Saptarshi Chakraborty², Yunqi Xi¹, Robert W. Bing¹, Huijuan Zhang¹, Xiaoyu Zhang³, Isabel Komornicki⁴, Linda M. Harris⁴, Wenyao Xu³ & Jun Xia¹✉

This study reports the first clinical longitudinal photoacoustic imaging (PAI) of chronic foot ulcers, a major complication in patients with peripheral vascular disorders. Compared to traditional methods such as ABI or near-infrared spectroscopy, the photoacoustic imaging approach provides non-invasive, high-resolution, and quantitative monitoring of vascular dynamics over time. Our system provided dorsal-side imaging of vascular structures with an expanded field of view and incorporated a skin artifact suppression algorithm to improve visualization of subdermal vasculature. From the acquired 2D and 3D images, we extracted a set of 45 quantitative features, representing signal intensity, texture complexity, and morphological changes associated with ulcer progression. Using a LASSO-based feature selection strategy, we identified the top-12 feature subset and validated them through multi-seed cross-validation. Our selection achieved an average classification accuracy of 79.6% and a macro-averaged AUC of 86.6% in distinguishing healing, worsening, and healthy cases. These findings demonstrate the clinical utility of photoacoustic biomarkers for personalized ulcer tracking and risk stratification.

Chronic foot ulcer is a significant medical concern that severely impacts patient mobility and quality of life¹. The chronic wounds, often associated with diabetes and peripheral arterial disease (PAD), are difficult to heal and require ongoing management to prevent complications such as infection, gangrene, and amputation². The increasing prevalence of foot ulcers imposes a substantial economic burden on healthcare systems due to the need for long-term wound care, frequent clinical monitoring, and hospitalizations. Despite advances in treatment, early and accurate assessment of ulcer progression remains a challenge, as traditional evaluation methods, including visual inspection and clinical scoring, are often subjective and insufficient for detailed analysis^{3,4}. In patients with diabetes or PAD in particular, impaired blood circulation is a common underlying cause of delayed or non-healing ulcers^{5,6}. An imaging technique that can directly visualize and quantify perfusion changes in vasculature is therefore essential for evaluating treatment efficacy⁷.

However, existing ulcer assessment modalities all come with distinct limitations. In routine wound care, handheld Doppler assessment and ABI/TBI are the most widely used tools for evaluating foot perfusion, but they provide only indirect indices that depend on operator experience and can be unreliable in patients with diabetes and medial

arterial calcification, offering limited spatial information on distal microcirculation⁸. In patients with diabetes, medial arterial calcification can lead to falsely elevated ABI values, which may underestimate the severity of peripheral arterial disease and limit its reliability in assessing distal foot perfusion. For this reason, the Toe-Brachial Index (TBI) is often recommended as a complementary measure to evaluate microvascular status in the foot^{9,10}. NIRS-based systems (e.g., Kent SnapshotNIR) can estimate oxy- and deoxyhemoglobin to assess microvascular perfusion, yet their accuracy is affected by skin pigmentation and tissue thickness, which may reduce robustness across diverse patient populations^{11,12}. Conventional imaging modalities such as X-ray and MRI are valuable for detecting complications (e.g., osteomyelitis, soft-tissue infection), but they are not designed for real-time, regional perfusion monitoring and are often costly or time-consuming^{13,14}. Duplex ultrasound primarily targets larger proximal arteries and is technically challenging at the foot level due to small, tortuous vessels and strict Doppler angle requirements, while angiography, although accurate for defining arterial occlusions, is invasive and unsuitable for frequent longitudinal follow-up¹⁵⁻¹⁷. Together, these limitations underscore the need for a noninvasive, repeatable imaging technique

¹Department of Biomedical Engineering, University at Buffalo, State University of New York, Buffalo, NY, USA. ²Department of Biostatistics, University at Buffalo, State University of New York, Buffalo, NY, USA. ³Department of Computer Science and Engineering, University at Buffalo, State University of New York, Buffalo, NY, USA. ⁴Department of Surgery, University at Buffalo, State University of New York, Buffalo, NY, USA. ✉e-mail: junxia@buffalo.edu

that can directly visualize and quantify local microvascular perfusion to guide foot ulcer assessment and treatment planning^{18–20}.

Advanced imaging technologies have been explored to improve ulcer assessment, with photoacoustic (PA) imaging emerging as a promising modality²¹. PA imaging (PAI) is a hybrid modality that integrates the high spatial resolution of ultrasound with the optical contrast of light, enabling detailed visualization of vascular structures and blood oxygenation²². However, most existing PA wound studies are either preclinical pressure-ulcer models in mice or small, short-term clinical feasibility studies, offering limited insight into standardized human implementation^{23,24}. For example, Hariri et al. demonstrated that PAI can noninvasively stage pressure ulcers and detect subclinical tissue damage in murine pressure ulcer models, while Mantri et al. showed that hybrid PA–ultrasound monitoring of angiogenesis over short weekly follow-up can stratify responders versus non-responders in small cohorts of chronic wounds^{23,25,26}. Overall, longitudinal human datasets are especially scarce: available protocols typically rely on 2D snapshots over brief follow-up periods, with small sample sizes, limited 3D coverage, and minimal quantitative feature extraction or outcome modeling^{23,27,28}. Because PA imaging uses non-ionizing light and ultrasound, it is safe, repeatable, and relatively cost-effective for serial bedside examinations, making it well-suited for tracking vascular and oxygenation changes in chronic ulcers^{29–31}. Rather than relying solely on static visual inspection, PA imaging can provide objective, time-resolved vascular information that supports earlier detection of deterioration and more informed therapeutic decisions³².

Building upon our previous work on the dual-scan foot imaging system³², this study represents the first longitudinal PAI study for quantitative and machine-learning-based outcome modeling of chronic foot ulcers. It establishes a standardized framework that enables repeated in vivo vascular imaging and outcome prediction over multiple clinical visits. To address the lack of quantitative tools for monitoring tissue perfusion using PA, we developed a comprehensive set of PA-based biomarkers spanning three categories: signal, texture, and morphology. These indicators capture changes in vascular signal quality and tissue structure during ulcer healing. By standardizing these measurements, the system offers a reproducible, objective method for evaluating ulcer progression over time, reducing reliance on subjective clinical assessments. The ability to extract quantitative biomarkers further enhances the system's clinical relevance by providing a structured framework for ulcer monitoring. Unlike traditional imaging studies that evaluate static images in isolation, this work emphasizes longitudinal tracking of each patient's vascular status across multiple timepoints. By comparing photoacoustic indicators before and after clinical interventions—such as surgery or wound care—the system enables individualized assessment of healing trajectories. This temporal approach improves sensitivity to change, reduces within-subject variability, and aligns with real-world clinical needs for monitoring treatment response. Collectively, this work represents a unique translational advance that integrates longitudinal imaging, quantitative vascular biomarkers, and predictive modeling—extending photoacoustic imaging from descriptive visualization to outcome-oriented clinical evaluation.

Results

Comparative analysis between healthy and patient groups

To identify key PA features, we ranked feature importance based on the averaged absolute LASSO coefficients from multiple one-vs-all models across random subject-level splits. This model-driven ranking highlighted the most discriminative features associated with healing, worsening, and healthy vascular trajectories. For healing or worsening patients, meaningful features were expected to exhibit temporal changes reflecting recovery or deterioration, while features in healthy individuals were assumed to remain stable, serving as controls for normal variation. As a result, the selected features capture both intra-subject physiological dynamics and cohort-level discriminative power. Based on this ranking, we systematically derived multiple Top-N feature subsets to evaluate how these biologically meaningful biomarkers translate into practical classification performance.

To identify an optimal balance between model sparsity and classification performance, we evaluated four feature set configurations: Top-6, Top-12, Top-24, and Top-45. As shown in Table 1, the Top-12 subset achieved the highest average accuracy (79.6%) and maintained balanced recall across the healing (83.0%), worsening (75.0%), and healthy (80.9%) groups. These results indicate strong generalization while preserving interpretability through feature sparsity. Although the Top-24 subset yielded a slightly higher macro AUC (89.4% vs. 86.6%), its average accuracy (77.5%) and healing recall (74.5%) were lower than those of Top-12, suggesting marginal gains in separability at the cost of clinical sensitivity. The Top-6 subset, despite its simplicity, suffered from poor recall in the worsening class (33.3%), potentially due to overfitting to dominant patterns while failing to capture minority class deterioration signals. In contrast, the Top-45 subset included many weakly informative features, resulting in the lowest overall accuracy (68.4%) and suboptimal recall for all three classes. These findings suggest that adding more features would not necessarily improve classification performance and may instead dilute the discriminative power of key features. Overall, the Top-12 configuration provides a favorable compromise between model compactness and robustness, supporting its use in downstream vascular outcome prediction tasks.

The final Top-12 features include vascular occupancy, SNR, vessel intensity and density, tissue heterogeneity, and 3D statistical descriptors—all of which reflect key vascular or tissue-level characteristics. These features were selected by ranking the aggregated absolute β coefficients across all training splits, ensuring consistent discriminative power and physiological interpretability. The model heavily relied on features associated with healing and worsening trajectories while assigning lower weights to healthy-related features, consistent with the minimal intra-subject variation expected in healthy subjects. Class-specific LASSO weights for these features are visualized in Fig. 1, which shows the averaged absolute $|\beta|$ coefficients across multiple train-test splits. These findings not only support the discriminative utility of the selected features but also highlight their clinical relevance for individualized ulcer monitoring and risk stratification.

Classification of healing, worsening, and healthy groups

To assess the predictive utility of the Top 12 model-driven vascular features, we trained a multi-class SVM classifier using subject-level hold-out validation. The input features were projected via LASSO-derived coefficients before classification, allowing each subject's longitudinal vector to be embedded into a sparse, discriminative subspace.

The classifier demonstrated strong generalization across repeated partitions. As shown in the macro-averaged ROC curve (Fig. 2a), the model achieved an AUC of 86.6%, confirming robust separability among healing, worsening, and healthy cohorts. The confusion matrix (Fig. 2b) provides a more granular view of class-level performance. Healing and healthy groups were accurately predicted in most cases (83.0% and 80.9%, respectively), reflecting clear vascular recovery and physiological stability. The worsening group showed moderate recall (75.0%) with some cases being misclassified as healthy. Importantly, no worsening case was misidentified as healing, indicating the model successfully detects signs of deterioration even when progression is subtle.

This lower recall in the worsening class may reflect the underlying imbalance in the dataset, where true worsening cases are clinically uncommon. In longitudinal ulcer monitoring, most patients tended to

Table 1 | Classification performance on the testing dataset using different numbers of Top feature sets

Top-N	Recall (Healing)	Recall (Worsening)	Recall (Healthy)	Avg. Accuracy	Macro AUC
6	83.0%	33.3%	85.1%	67.1%	88.0%
12	83.0%	75.0%	80.9%	79.6%	86.6%
24	74.5%	75.0%	83.0%	77.5%	89.4%
45	72.3%	58.3%	74.5%	68.4%	81.5%

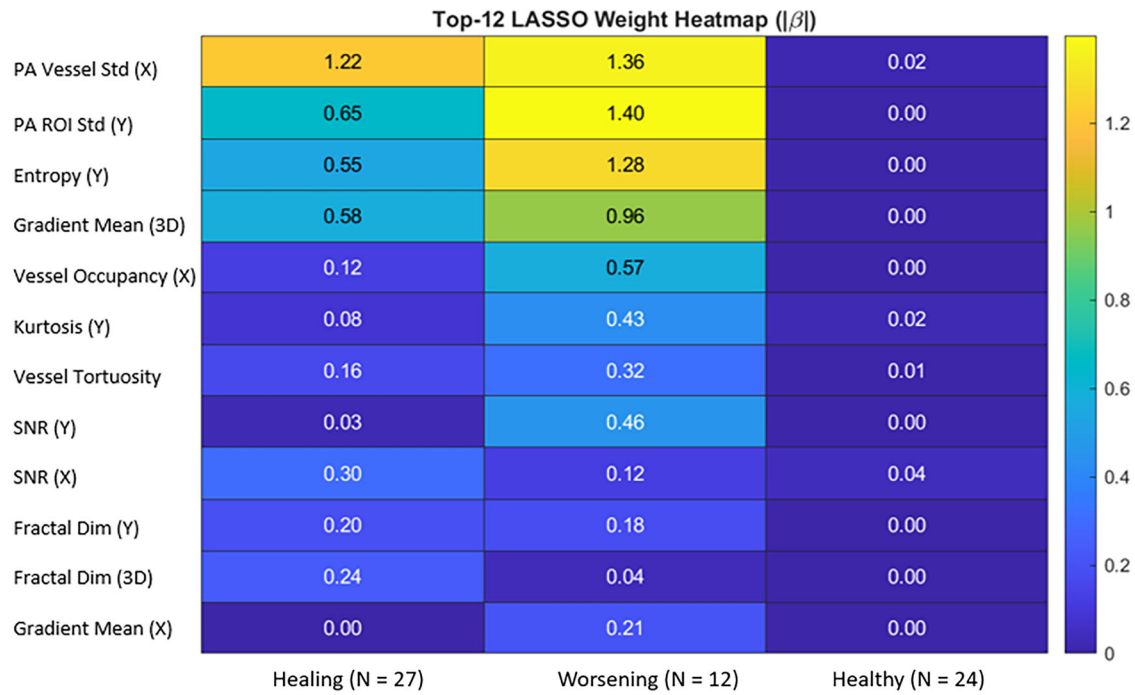


Fig. 1 | Class-specific LASSO weight heatmap ($|\beta|$) for the Top-12 model. The heatmap shows the absolute LASSO coefficients ($|\beta|$) of the Top-12 features for the three outcome classes (healing, worsening, healthy). Warmer colors (yellow to light green) indicate larger coefficients, whereas cooler colors (blue to dark blue) indicate

smaller coefficients. Feature names are listed on the y-axis and outcome classes on the x-axis, with class sample sizes shown below the axis (Healing: $n = 27$; Worsening: $n = 12$; Healthy: $n = 24$).

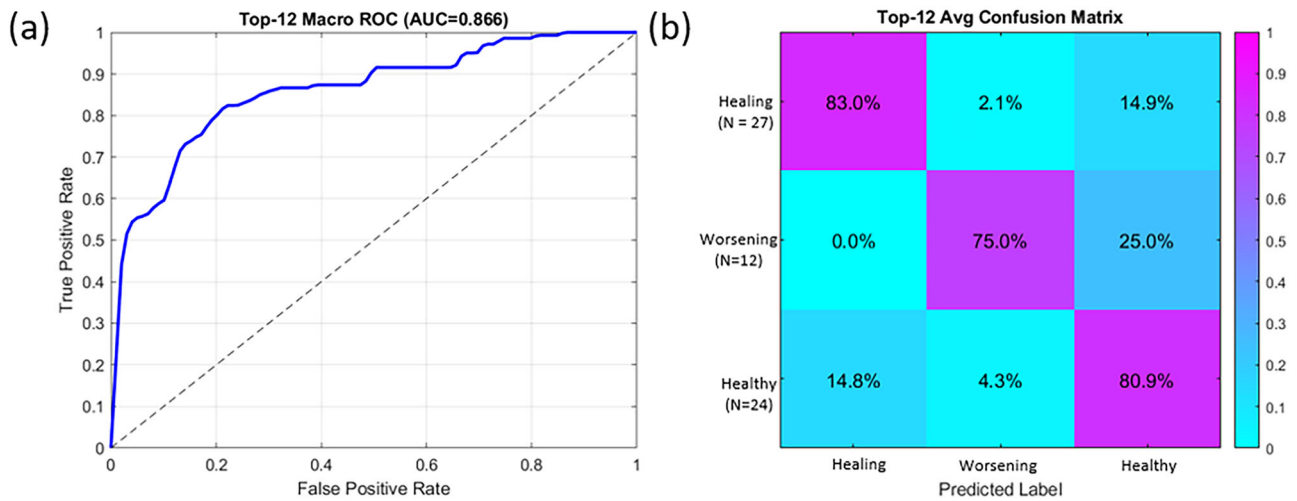


Fig. 2 | Performance of the Top-12 LASSO-SVM classifier. **a** Macro-averaged ROC curve for the Top-12 model; the blue solid line indicates the macro-averaged ROC and the gray dashed line indicates the diagonal reference (no-skill) classifier. **b** Averaged confusion matrix for the Top-12 feature model across 10 random

train-test splits. The color scale from cyan to magenta represents the averaged classification accuracy (proportion of samples) in each cell, with magenta indicating higher values and cyan indicating lower values. Healing: $n = 27$; Worsening: $n = 12$; Healthy: $n = 24$.

improve with medical intervention, while only a small subset experienced continued vascular deterioration. As a result, the training data for the worsening class was limited in size, which could have constrained the model’s ability to generalize to this group. Nevertheless, the classifier achieved high precision for worsening cases and maintained strong overall group-level discrimination, as supported by both ROC and confusion matrix evaluations. These findings validate the utility of selected photoacoustic features for tracking vascular dynamics and support the feasibility of outcome classification in ulcer monitoring workflows.

Across the 10 randomized train-test splits, the Top-12 LASSO-SVM model exhibited consistent performance, with bootstrap-derived 95% confidence intervals indicating relatively narrow uncertainty around the reported test accuracy and macro AUC. Label permutation testing (5000 iterations) further confirmed that these metrics are highly unlikely to occur by chance ($p \ll 0.01$ for both accuracy and macro AUC).

Physiological validation of longitudinal feature changes

To further validate the physiological relevance of the model-selected features, we analyzed the within-subject temporal changes (Δ) for each

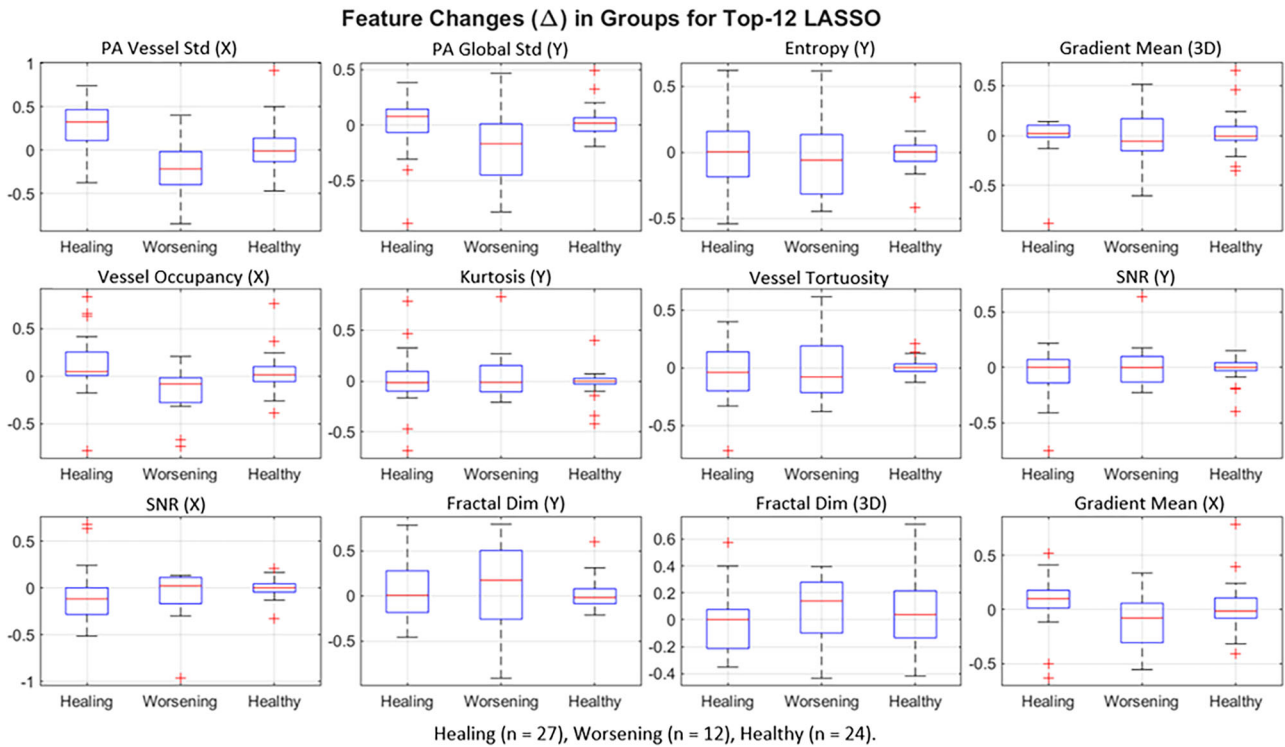


Fig. 3 | Box plots of within-subject changes (Δ) for the Top-12 LASSO-selected features across clinical groups. For each subplot, the blue box indicates the interquartile range, the red horizontal line indicates the median, the whiskers indicate the

1.5 \times interquartile range, and red crosses indicate outliers. Healing: $n = 27$; Worsening: $n = 12$; Healthy: $n = 24$.

of the 12 Top-ranked PA features. For each subject, we computed the difference in feature values between the first and second imaging sessions and compared these changes across the healing, worsening, and healthy cohorts.

Figure 3 illustrates the distribution of longitudinal changes (Δ) in the Top-12 LASSO-selected features across the three clinical groups. While individual features demonstrated varying degrees of separation across groups, consistent directional trends were observed in several vascular metrics. Features such as PA Global Std (Y), Vessel Occupancy (X), and Fractal Dimension (3D) showed clear inter-group distinctions, with changes that reflect vessel signal heterogeneity and spatial occupancy dynamics during ulcer progression. Conversely, some features showed greater variability within groups. For example, Kurtosis (Y) and Entropy (Y) often exhibited outliers and wide value ranges. These variations likely result from localized signal fluctuations and minor differences during image quantification. Beyond overall dispersion, morphology-related descriptors further clarify these trends. In our data, fractal dimension tended to decrease in healing subjects and increase in worsening cases, indicating that clearer, better-organized vascular trees are associated with recovery, whereas more tortuous, fragmented, and structurally complex patterns are characteristic of progressive ischemia. Entropy showed small but directionally consistent shifts in the ulcer groups: it tended to increase slightly in healing subjects and decrease slightly in worsening subjects, whereas healthy volunteers showed changes clustered tightly around zero, indicating stable background heterogeneity over time.

Among all features, three—Vessel Occupancy (X), PA Vessel Std (X), and Gradient Mean (X)—demonstrated particularly interpretable trends consistent with known vascular mechanisms in chronic wound physiology. Increased vessel occupancy in healing subjects likely reflects enhanced microvascular perfusion and angiogenesis, whereas reduced occupancy in worsening cases may suggest persistent ischemia^{33–35}. Gradient Mean (X) appeared elevated in cases with clearer and denser vascular structures. This may reflect sharper vessel boundaries and

increased structural definition, which are consistent with microvascular remodeling and enhanced perfusion patterns^{36–38}. Meanwhile, increased PA vessel signal standard deviation in healing subjects may reflect dynamic microvascular remodeling, where newly formed vessels introduce local signal variability during tissue reperfusion. Similar heterogeneity in blood flow distribution has been noted in perfusion studies using CT and MRI, where regional variance in enhancement patterns often signals active angiogenesis or transitional vascular states during recovery^{39–41}.

In addition, we further summarized the clinical implications of these key photoacoustic parameters in the *Discussion* section. In general, an increase in vessel occupancy or gradient mean suggests enhanced vascular filling, sharper vessel boundaries, and improved perfusion, consistent with tissue recovery and healing. Conversely, a decrease in these parameters often indicates reduced perfusion and vascular rarefaction associated with ischemic deterioration. Nevertheless, individual parameters alone cannot serve as absolute diagnostic indicators; their longitudinal combination provides a more comprehensive and reliable representation of ulcer progression.

To quantify groupwise differences in Δ -features, we applied a non-parametric Kruskal–Wallis test across the three clinical groups for all twelve Top-12 features and applied epsilon-squared (ϵ^2) as an effect size measure. Five features—PA Vessel Std (X), PA Global Std (Y), Vessel Occupancy (X), SNR2D (X), and Gradient Mean (X)—showed statistically significant differences among healing, worsening, and healthy subjects ($p < 0.05$), with small-to-moderate effect sizes for most metrics ($\epsilon^2 \approx 0.07$ – 0.14) and a larger effect for PA Vessel Std (X) ($\epsilon^2 \approx 0.27$). The complete set of p -values for all twelve Δ -features is summarized in Tables S1 and S2.

Overall, these results highlight that single features alone are insufficient as static diagnostic thresholds. Instead, they reinforce the need for patient-specific, longitudinal analysis using multiple complementary features, which will provide a more robust and individualized assessment of ulcer progression.

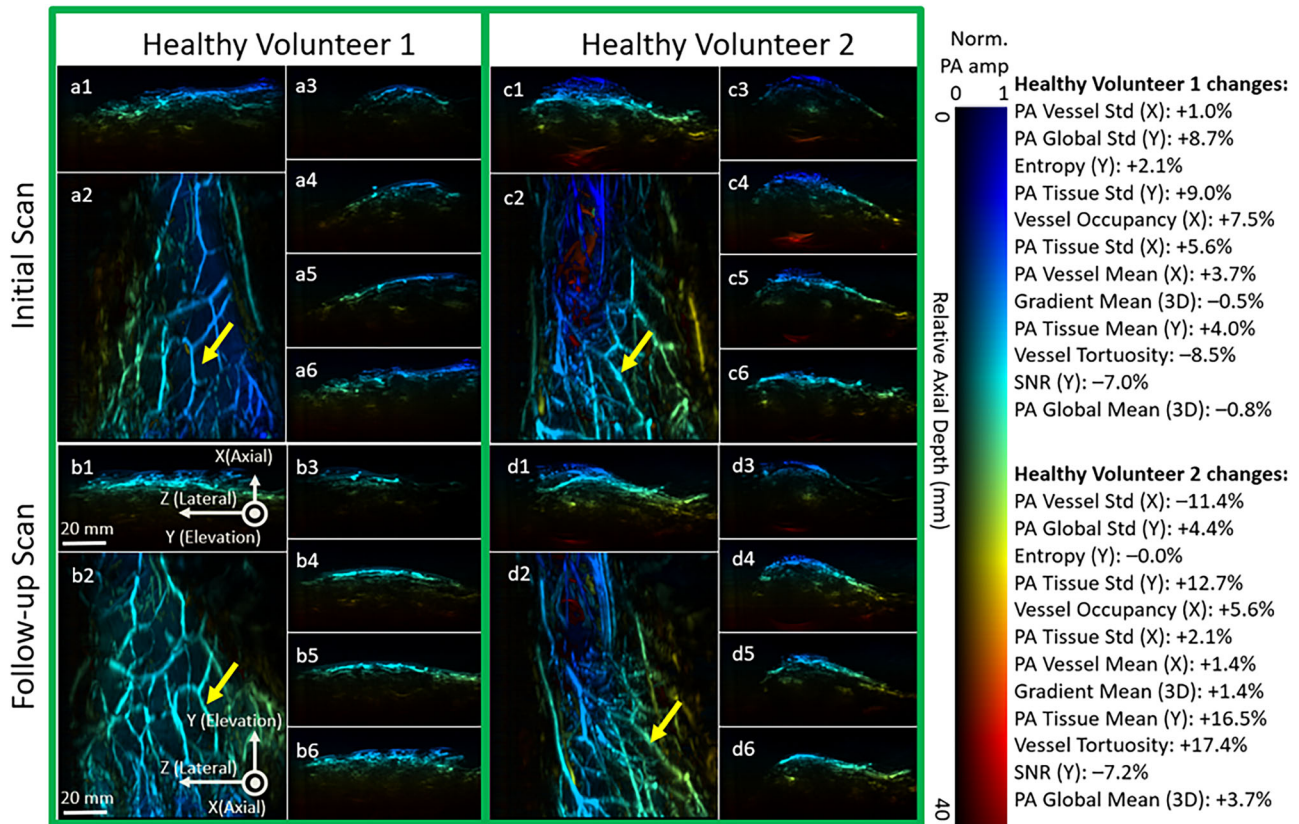


Fig. 4 | Longitudinal vascular imaging in healthy volunteers. (a1–a6) Multi-view initial scan of Healthy Volunteer 1; (b1–b6) corresponding follow-up scan of the same subject. (c1–c6) Initial scan of Healthy Volunteer 2; (d1–d6) corresponding follow-up scan of the same subject. Yellow arrows highlight corresponding vessel segments across the two time points in healthy feet. The color map encodes relative

axial depth, with blue indicating superficial vessels (0 mm) and red indicating the deepest reconstructed vessels (40 mm). Brighter colors represent higher photoacoustic signal amplitude, whereas darker colors indicate lower signal amplitude. All images demonstrate consistent vascular structures and minimal variation across time points. Quantitative feature changes are summarized on the right.

Longitudinal reproducibility and predictive consistency in subjects

To further illustrate the system’s performance at the individual level, we examined longitudinal scans from six representative subjects. Specifically, two healthy volunteers were imaged at two separate time points to examine temporal stability, two patients with healing ulcers were scanned during the active disease stage and again after visible clinical improvement, and two patients with worsening ulcers were imaged at baseline and at a later visit demonstrating further vascular deterioration.

In both healthy subjects, vascular patterns remained visually consistent across scans, with no qualitative anatomical or perfusion-related changes (Fig. 4). Quantitatively, features such as 2D SNR, vessel intensity, occupancy, and texture metrics showed only modest fluctuations (typically within ±10–15%) and no systematic directional drift, consistent with stable vascular status rather than true remodeling. Prediction probabilities in Table 2 reflect this stability: Subject 01 received 84.8% probability for “healthy” and Subject 02 reached 68.3%, both with 10/10 model agreement. These findings confirm high intra-subject reproducibility under unchanged physiological conditions.

In contrast, healing subjects exhibited marked vascular improvements between scans (Fig. 5). Vessel structures appeared clearer, intensity levels increased, and tissue-related noise decreased. Previously blurred distal branches became sharper and more easily distinguishable, and the continuity of small vessels improved along both the Y (elevation) and Z (lateral) directions. Features such as vessel intensity, tissue gradient, and vessel tortuosity showed substantial increases. Overall, PA signal intensity within the vascular arc increased, with finer vessels no longer merging into the background, consistent with clearer vascular definition and strengthened perfusion in the ulcer region. Table 2 further supports this progression—

Table 2 | Model prediction results for individual subjects

Subject ID	Average probability healing	Average probability worsening	Average probability healthy	Prediction consensus (10 seeds)
Healthy 01	11.9%	3.3%	84.8%	10/10
Healthy 02	28.5%	3.2%	68.3%	10/10
Healing 01	72.6%	3.7%	23.6%	10/10
Healing 02	72.6%	3.7%	23.6%	10/10
Worsening 01	11.2%	69.4%	19.4%	10/10
Worsening 02	8.3%	77.6%	14.1%	10/10

Healing Subject 01 was classified as “healing” with 72.6% probability, and Subject 02 reached 85.9%, both with unanimous voting. These results highlight the system’s ability to detect meaningful recovery-related changes through both image features and classification outputs.

Two representative worsening cases are shown in Fig. 6. In contrast to the healing cases, these subjects exhibited a progressive loss of coherent vasculature between the initial and follow-up scans. Distal branches became more fragmented and faded into a diffuse background, and the main vessel trunks appeared flatter and less well defined. Within the ulcer region, PA vessel and tissue intensities and their standard deviations decreased overall, and vessel occupancy in the elevation direction dropped by roughly 25–40%, consistent with a sparser and more discontinuous vascular bed. Gradient-based and texture features likewise tended to decline, in line with the smoother, less structured appearance of the tissue–vessel interface, whereas

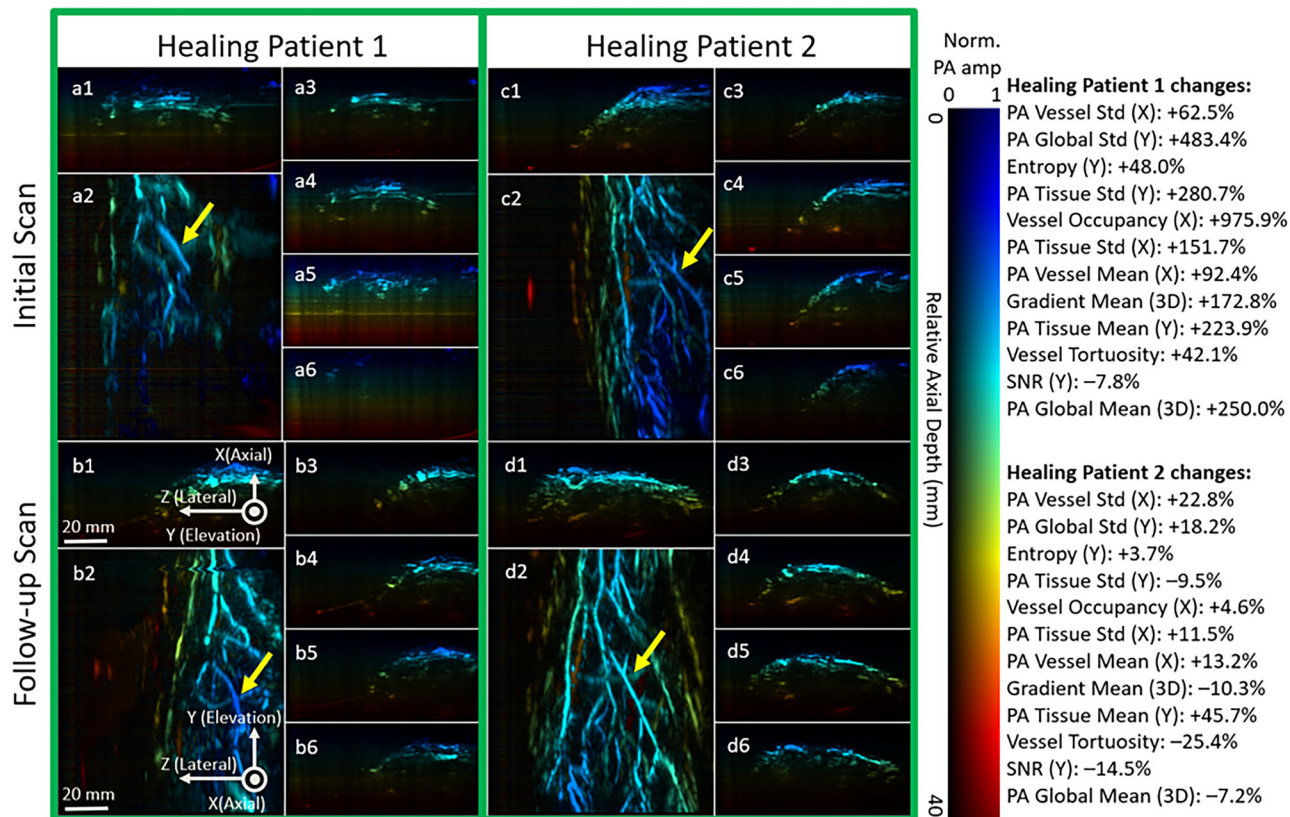


Fig. 5 | Longitudinal vascular changes in healing patients. (a1–a6) Multi-view initial scan of Healing Patient 1; (b1–b6) follow-up scan of the same patient showing enhanced vessel continuity and intensity. (c1–c6) Initial scan of Healing Patient 2; (d1–d6) follow-up scan of the same patient with visible vascular remodeling. Yellow arrows highlight corresponding vessel segments across the two time points in

healing feet. The color map encodes relative axial depth, with blue indicating superficial vessels (0 mm) and red indicating the deepest reconstructed vessels (40 mm). Brighter colors represent higher photoacoustic signal amplitude, whereas darker colors indicate lower signal amplitude. Quantitative feature changes are summarized on the right.

changes in SNR were comparatively modest. Table 2 reflects this deterioration: Worsening Subject 01 reached a mean worsening probability of 69.4%, and Subject 02 increased to 77.6%, both with unanimous voting, indicating that the longitudinal PA features predominantly support a worsening trajectory rather than recovery.

These six longitudinal cases demonstrate that the system performs reliably across stable, healing, and worsening trajectories. In healthy volunteers, vascular features and predicted probabilities remained stable over time, whereas in healing and worsening patients, the classifier followed the expected clinical course, with increasing “healing” probability in cases showing improved perfusion and increasing “worsening” probability when microvascular pruning and signal loss were observed. Although the magnitude of individual feature changes varied between subjects, all six predictions were consistent with the physicians’ clinical assessments and supported by unanimous agreement across all seeds. The corresponding probabilities and feature trajectories are summarized in Table 2.

Discussion

The key PA features identified by our model integrate signal-, texture-, and morphology-based characteristics, reflecting the multi-dimensional nature of vascular changes in ulcer progression. By focusing on intra-subject differences over time rather than static absolute values, this approach provides individualized assessments. This design improves the interpretability of vascular dynamics^{42,43}. Signal-based metrics—such as SNR (X/Y), PA vessel standard deviation (X), and vessel occupancy (X)—often increased in healing subjects while remaining stable in healthy individuals, suggesting associations with improved perfusion or vascular signal enhancement during recovery. Texture descriptors, including gradient mean (3D/X), PA

global/ROI standard deviation (Y), and entropy (Y), captured subtle changes in structural complexity and image heterogeneity that accompany tissue remodeling. Morphological features such as vessel tortuosity and fractal dimension (Y/3D) contributed complementary insights into the geometric adaptations of vascular networks near ulcer sites. Taken together, these findings underscore that no single domain could sufficiently explain ulcer progression; instead, a multi-domain, longitudinal perspective provides a more robust and physiologically meaningful basis for outcome stratification.

The SVM model achieved strong overall performance, with a hold-out accuracy of 79.6% and a macro-averaged AUC of 86.6% across subject-level evaluations. It effectively separated healing, worsening, and healthy cases based on longitudinal changes in vascular features. Classification errors primarily occurred between healing and worsening groups, likely due to overlapping vascular patterns and intermediate recovery stages. This remains a common challenge in clinical ulcer assessment⁴⁴. The relatively lower recall for worsening cases (75.0%) suggests difficulty in capturing this group’s heterogeneity, potentially due to limited sample diversity. In contrast, healing cases were more consistently identified (83.0% recall), due to the larger sample size. These findings emphasize the need to expand the worsening cohort and refine discriminative features such as SNR, gradient mean, and vessel tortuosity to better handle borderline cases in future applications.

The Top-12 LASSO–SVM classifier demonstrated stable behavior across independent train–test splits, with a mean test accuracy of 79.6% and a macro AUC of 86.6%, accompanied by relatively tight bootstrap-derived 95% confidence intervals, indicating that performance did not hinge on a single favorable partition. Permutation testing further yielded very low p-values for both accuracy and macro AUC, suggesting that the observed

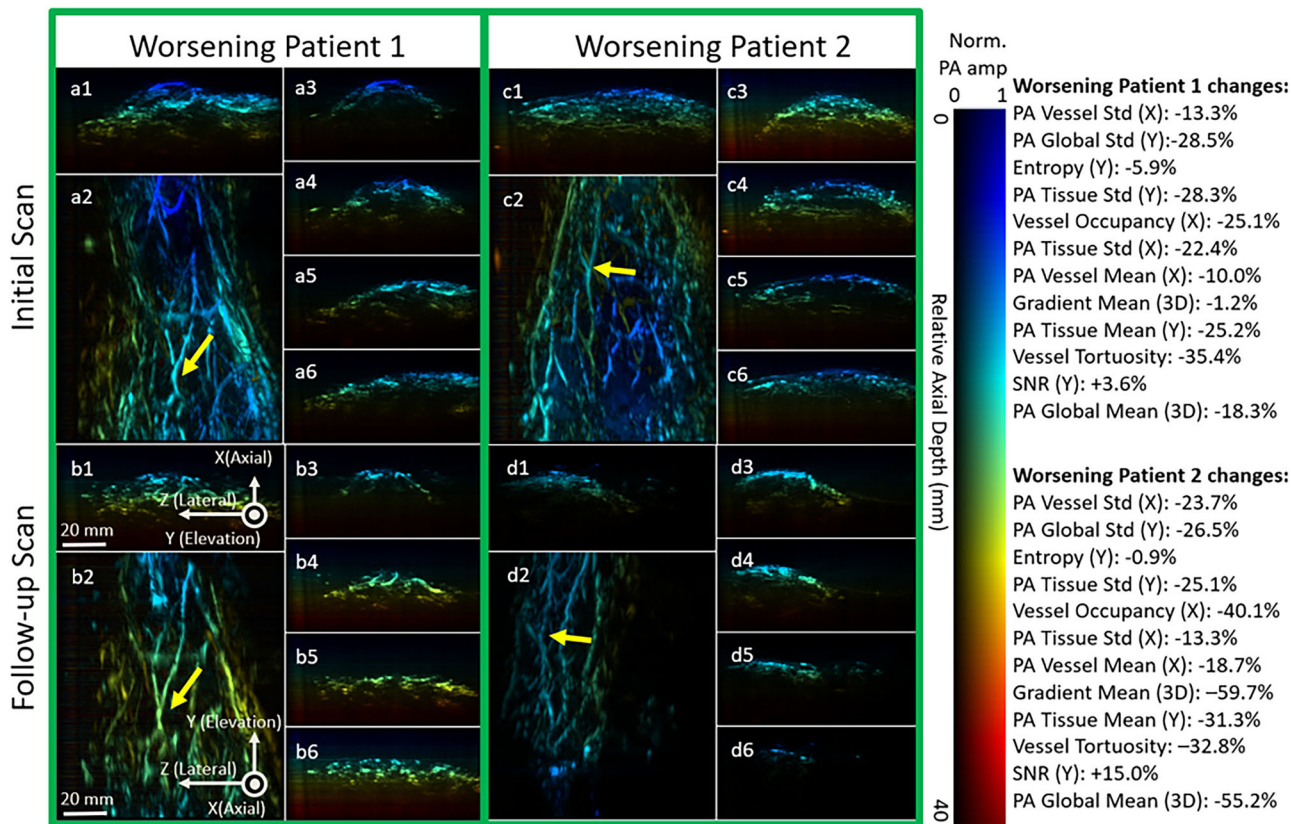


Fig. 6 | Longitudinal vascular changes in worsening patients. (a1–a6) Multi-view initial scan of Worsening Patient 1; (b1–b6) follow-up scan of the same patient showing reduced vessel continuity and attenuated PA signal intensity. (c1–c6) Initial scan of Worsening Patient 2; (d1–d6) follow-up scan of the same patient with further loss of small branching vessels and a more diffuse vascular pattern. Yellow arrows

highlight corresponding vessel segments across the two time points in worsening feet. The color map encodes relative axial depth, with blue indicating superficial vessels (0 mm) and red indicating the deepest reconstructed vessels (40 mm). Brighter colors represent higher photoacoustic signal amplitude, whereas darker colors indicate lower signal amplitude. Quantitative feature changes are summarized on the right.

discrimination is unlikely to arise from random label assignments. At the same time, the width of the confidence intervals still reflects the modest cohort size and the need for larger, multi-center validation. Consistent with this picture, the groupwise analysis of Δ -features showed that only a subset of the twelve Top-ranked parameters exhibited statistically significant differences among healing, worsening, and healthy subjects, with small-to-moderate effect sizes for most metrics and a larger effect for PA vessel standard deviation. This pattern reinforces that no single longitudinal descriptor is sufficient as a stand-alone biomarker; instead, each feature captures a complementary facet of vascular remodeling or ischemic deterioration, and their combined, delta-based representation provides a more physiologically coherent summary of ulcer trajectories for classification.

Compared to traditional methods such as ABI and TBI, PA imaging offers distinct advantages by directly visualizing vascular structures and capturing high-resolution signal and texture features over time⁴⁵. Its ability to detect microvascular changes and quantify longitudinal trends enables patient-specific tracking of ulcer progression. Indicators such as vessel occupancy, SNR, and gradient-based features demonstrated consistent trends aligned with clinical outcomes, supporting their potential as interpretable, image-based biomarkers. The 3D imaging approach further enhances spatial specificity and reduces ambiguity from superficial artifacts. Nonetheless, PA imaging remains sensitive to factors such as skin pigmentation and reduced signal quality in deeper tissue layers²⁶. In addition, minor variations in foot positioning between longitudinal sessions may occur. However, since our analysis focused on regional or global ROIs and relative longitudinal trends rather than absolute vessel positions, such variations have minimal impact on the overall results. Other potential limitations include the assumption of a uniform sound speed during reconstruction and variability in optical illumination due to surface

curvature. These factors may introduce minor fluctuations in signal intensity or sharpness, but their impact is mitigated by the longitudinal and multi-feature design of this study. Future work will incorporate adaptive sound-speed correction and laser output monitoring schemes to further improve quantitative accuracy. Finally, morphological descriptors like vessel tortuosity and fractal dimension were sometimes less reliable in fragmented vascular regions near ulcers. Future work will incorporate vessel-graph regularization and length/SNR-based segment filtering before computing tortuosity or fractal metrics, so that these descriptors are derived from stable, physiologically meaningful trunks rather than fragmented branches.

Currently, the ground truth of healing/worsening was defined by vascular specialists who integrated ABI/TBI readings (when available), Doppler assessment, and direct wound examination. This comprehensive approach reflects actual clinical practice, ensuring that the evaluation of PA-derived biomarkers aligns with real-world diagnostic decision-making. Future work may incorporate additional perfusion assessment modalities—such as transcutaneous oxygen measurement or hyperspectral imaging—to further corroborate clinical judgments and strengthen the reliability of PA-based biomarkers. Moreover, although no universal gold standard exists for quantifying foot microvascular structure, larger-scale studies could validate the quantitative accuracy of vessel-level parameters using CT angiography and/or digital subtraction angiography (DSA). Such validation would anchor PA-derived vascular metrics to absolute anatomical dimensions and enhance their clinical relevance.

Beyond the system- and clinic-level enhancements described above, our next steps will focus on increasing the sample size—especially for the worsening cohort—to improve model generalizability and mitigate performance bias. A larger and more balanced cohort will also enable

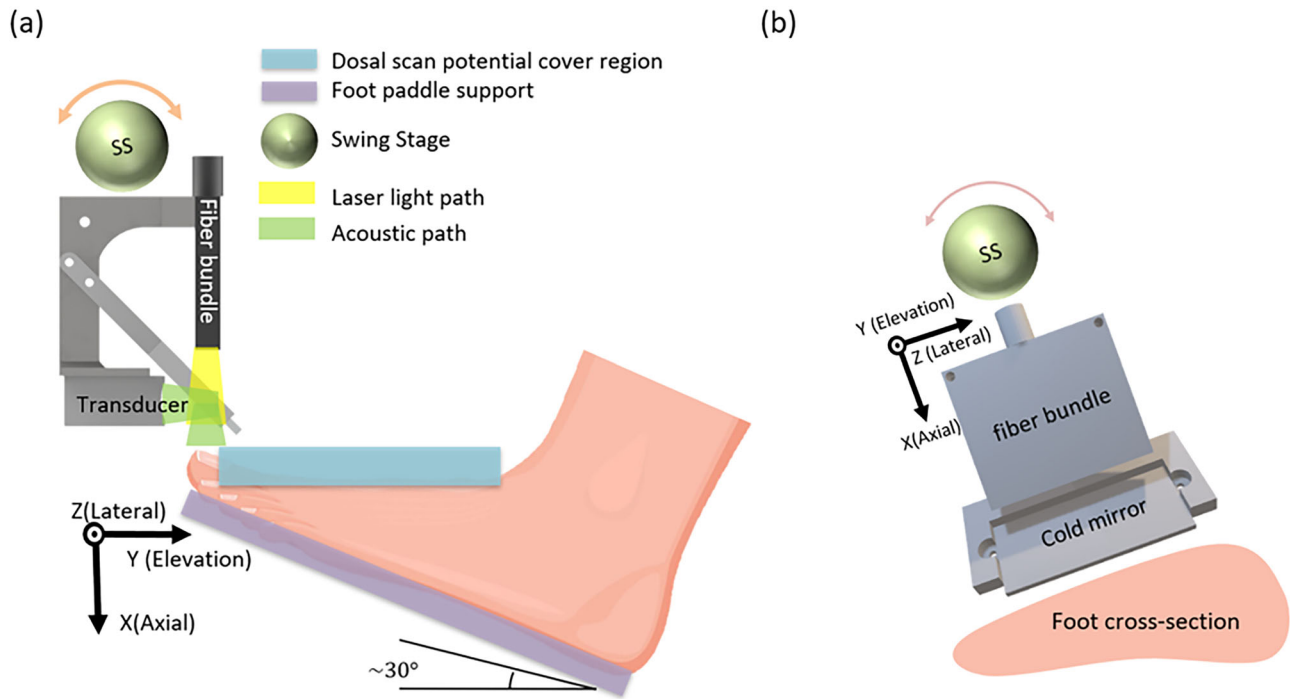


Fig. 7 | Schematic of the PA imaging system. a Side view of the system setup. **b** Front view of system setup.

systematic evaluation of potential confounders such as follow-up interval, age, and sex within the statistical framework. These analyses will help determine whether temporal spacing between visits or age- and sex-related vascular variability would influence feature distributions or classification outcomes. Their potential systematic impact between clinical groups will be quantified in future studies with larger test–retest cohorts. Additionally, we will capture pre- and post-surgery scans from the same patients to evaluate surgical impact on vascular recovery, providing a more comprehensive view of treatment response. Lastly, we aim to develop an AI-based interpreter that can explain the clinical relevance of PA features, thereby enhancing model transparency and facilitating integration into routine wound care workflows⁴⁶.

This study presents the first clinical evaluation of a longitudinal photoacoustic imaging framework for chronic foot ulcers. By combining dorsal-side PACT scanning, motion-adaptive acquisition, and automated skin removal, the system offers consistent vascular imaging across visits. From 45 candidate features, a robust subset of 12 features was selected using multi-seed LASSO and validated through SVM classification, achieving 79.6% accuracy and 86.6% macro AUC in stratifying healing, worsening, and healthy trajectories.

The analysis emphasized intra-subject vascular changes over time, improving sensitivity to progression while reducing anatomical variability. Key features such as SNR, occupancy, and gradient-based metrics demonstrated high discriminative and physiological relevance. Compared to ABI or TBI, PA imaging uniquely enables 3D, non-invasive monitoring of perfusion dynamics. Despite limitations in morphological stability and signal sensitivity in deep tissue, PA-derived biomarkers show strong potential for individualized ulcer tracking, risk assessment, and clinical decision support.

Methods
Imaging procedure

To improve usability and clinical applicability based on our previous work³², we refined our PA imaging system by focusing on the dorsal side of the foot. This region is clinically relevant since ischemic ulcers in PAD patients often develop at the toes and dorsal forefoot, where perfusion compromise is most pronounced. In addition, the dorsal aspect provides a consistent and

accessible site for standardized imaging, facilitating integration into routine vascular assessment workflows.

To enhance image quality and patient comfort, the top water tank was redesigned with a larger flexible film that conforms to the foot, which improves acoustic coupling. The field of view (FOV) was expanded from 50 mm × 86 mm to 100 mm × 86 mm to accommodate a broader range of foot sizes, thereby improving feature extraction reliability. A swing stage was integrated into the top imaging system to address anatomical variation and enhance scanning consistency, as shown in Fig. 7a, b. The swing stage is a ball-joint-based adjustable mount that allows broad angular adjustment (approximately ±90°) along the lateral axis, enabling fine alignment between the transducer and the curved dorsal foot surface. Once the optimal orientation is roughly achieved, the stage can be mechanically locked to prevent motion during scanning, ensuring geometric stability and reproducibility across longitudinal sessions. This structure allows the transducer to follow the foot curvature, maintaining a stable scanning surface and reducing motion artifacts. Additionally, a foot-stepping paddle was introduced to assist patients in maintaining a comfortable and consistent posture throughout the scan, supporting stable longitudinal monitoring. The scanning head uses a 128-element linear-array transducer (2.25 MHz) with curved elements for acoustic focusing, vertically aligned with the fiber bundle, and a 45-degree cold mirror for co-planar light illumination and detection. This setup enables deep tissue penetration and high spatial resolution. These refinements collectively improve ease of use, reduce variability in patient positioning, and ensure high-quality, reproducible vascular imaging. During all acquisitions, the laser output power was kept stable at approximately 2.7 W to maintain a consistent optical fluence at the tissue surface.

To ensure consistent imaging of the same anatomical region across longitudinal sessions, a customized foot holder was used to maintain a stable orientation of the foot relative to the scanning probe. The probe was mounted on a motorized linear stage with a fixed coordinate origin and a lateral field of view of approximately 86 mm, covering the entire dorsal foot region. The stage translated at a constant speed of 2 mm/s, synchronized with the 10 Hz laser repetition rate, producing a uniform B-scan spacing of 0.2 mm. This spacing was smaller than the system’s elevation resolution of 1.2 mm, thereby ensuring dense and consistent spatial sampling during 3D

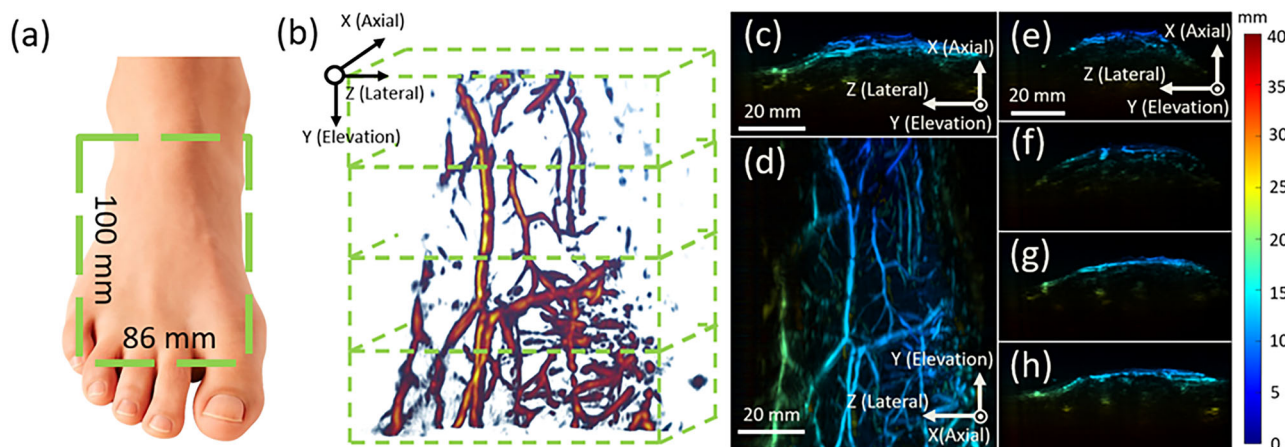


Fig. 8 | PA imaging and 3D vascular reconstruction. **a** Illustration of a foot with a 100 mm × 86 mm imaging field marked by a green dashed box. **b** Volume rendering with 3D axis annotation surrounded by a green dashed box. **c** Lateral–Axial

(XZ) MAP projection. **d** Elevation–Lateral (YZ) MAP projection. **e–h** Sub-volume MAP views in the XZ projection. Each volume corresponds to a dashed green box in **b**.

image construction. During each follow-up session, the operator aligned the scan using stable anatomical landmarks, such as the toe bases and ankle contour, and verified the field of view by matching characteristic vascular patterns. Because this study emphasized relative longitudinal changes rather than absolute registration, this alignment protocol was sufficient for reliable dynamic comparison. The imaging resolution of the system was characterized using a 0.2 mm cross-line phantom, from which the lateral and axial resolutions were determined by the full width at half maximum (FWHM) of photoacoustic amplitude profiles. The measured resolution was approximately 0.8 mm in lateral and 1.2 mm in elevation, consistent with the system's design specifications³².

All PA data were processed offline using a custom MATLAB-based pipeline. Raw signals from the dorsal-aspect system were filtered with a 1–5 MHz bandpass filter to suppress system noise. Image reconstruction was performed using a 2D back-projection algorithm with a constant speed of sound of 1.51 mm/μs. Each reconstructed B-scan corresponds to a single laser pulse synchronized with the motor position. After reconstruction, Hilbert envelope detection was applied to convert the bipolar signals into unipolar magnitude images. The 2D frames were stacked sequentially along the scanning (Y) axis according to their physical acquisition order and spacing (0.2 mm) to form a 3D volume. The acoustic coupling water was maintained at a constant temperature of approximately 21 °C using a built-in heater and temperature controller, ensuring stable sound-speed conditions across all imaging sessions. The resulting 2D frames were stacked along the scanning axis to generate a volumetric 3D image. As shown in Fig. 8, the reconstructed data were visualized for both anatomical reference and downstream analysis. Figure 8a displays the scanned foot with the imaging region marked (100 mm × 86 mm) by a green dashed box, and Fig. 8b shows the full 3D volume rendering with coordinate axes. To examine vascular structures from orthogonal perspectives, we first indicate the dorsal field of view (100 × 86 mm) in Fig. 8a. The axis-annotated 3D volume in Fig. 8b establishes the viewing axes and defines four sub-volume boundaries along the elevation (Y) direction. Figure 8c presents a maximum amplitude projection (MAP) along the axial-lateral (XZ) plane, while Fig. 8d shows a MAP view along the elevation-lateral (YZ) plane. For the XZ plane MAP, due to the long scanning distance, we divided the data into four sub-volumes along the scanning (Y) axis, as shown in Fig. 8b. The corresponding MAP views for each section are shown in Fig. 8e–h, respectively. These segmented regions and MAPs are used for feature extraction and classification.

Subjects with darker skin tones often exhibited elevated surface signal²⁶. To address this, we implemented a skin-removal algorithm that allows the user to manually define skin contours in both axial-lateral (XZ) and

elevation–lateral (YZ) views³². These contours are used to generate a 3D skin mask, which is then applied to the reconstruction volume to selectively suppress superficial signals while preserving subdermal vasculature.

Clinical workflow

Clinicians first prescreened patients to identify foot ulcers primarily caused by tissue ischemia. During the office visit, our collaborating physicians or nurse practitioners explained the study and confirmed each patient's willingness to participate. For those who agreed, PA imaging was then performed by our team immediately after the clinical appointment, minimizing disruption to routine care and enabling consistent longitudinal monitoring. Before scanning, patients were positioned using a swing stage and foot paddle for repeatable foot placement. Once aligned, a dorsal-aspect scan covering 86 mm in width and 100 mm in length was completed in approximately 50 s. Raw data were processed offline with bandpass filtering and back-projection reconstruction. The reconstructed volumetric data then underwent image preprocessing, including skin artifact suppression, intensity normalization, and noise reduction to improve image quality prior to segmentation. For follow-up visits, the extracted features were compared longitudinally with previous scans to quantify vascular changes and evaluate treatment progression. Finally, the results were interpreted in a clinical context to assess ulcer healing status or post-surgical recovery, and then documented for follow-up. A schematic representation of this workflow is illustrated in Fig. 9.

Patients

This study involved 39 patients with chronic foot ulcers and 24 healthy volunteers. Data collection is ongoing, and the present analysis is based on data collected up to May 2025. All participants underwent PA imaging at multiple time points for longitudinal data analysis. Participants were adults (≥18 years) with chronic foot wounds presumed to result from arterial insufficiency or gangrene. Patients with massive deep-tissue infection or nearby skin conditions (e.g., melanoma, psoriasis) were excluded. Tissue ischemia was prescreened using ABI/TBI when available and assessed by the treating physician during the scheduled visit.

A comprehensive demographic summary is presented in Table 3, based on baseline assessments from the full cohort ($N = 63$). Among all 63 subjects, there are 35 females (55.6%) and 28 males (44.4%). The racial composition comprised 47 participants identifying as White (74.6%), 15 as Asian (23.8%), and 1 as African American (1.6%). Subjects' ages ranged from 22 to 89 years, with an overall mean of 59.3 ± 19.2 years. The patient group ($N = 39$) included 22 females (56.4%) and 17 males (43.6%). Of these, 27 were categorized as healing and 12 as worsening, based on clinical trajectories and follow-up outcomes. The majority of patients (94.9%)

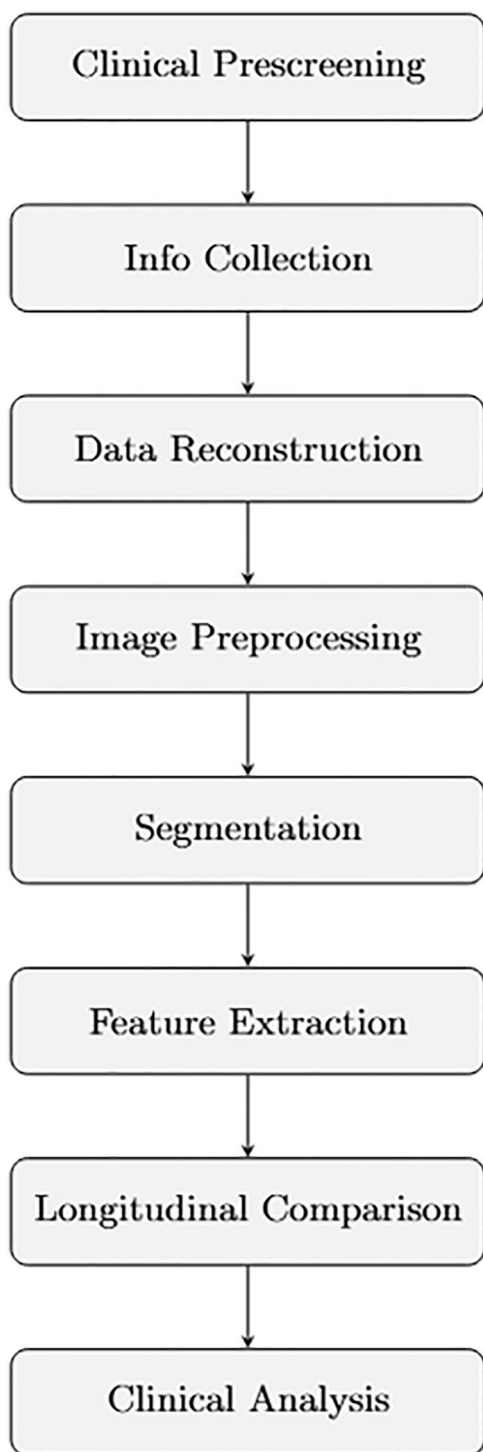


Fig. 9 | Schematic of the integrated workflow for patient screening, photoacoustic imaging, and longitudinal outcome analysis.

identified as White ($n = 37$), with the remaining 2 identifying as Asian. Their ages ranged from 47 to 89 years, with a mean of 69.0 ± 10.3 years. Each patient underwent at least two PA imaging sessions, with intervals varying from a few days to several months, depending on individual clinical follow-up schedules. These follow-up intervals reflected routine vascular clinic practice and were determined by the treating physicians based on each patient’s condition, rather than by a fixed research protocol. As a result, the timing of PA imaging was heterogeneous across subjects, ranging from short-interval reassessments after acute changes to longer-term surveillance of stable wounds.

Table 3 | Summary of patient characteristics

	Healing group	Worsening group	Healthy group
Total Count	27	12	24
Age Mean	66.4	74.7	43.5
Age Std	10.5	7.4	19.9
Age Min	47	62	22
Age Max	89	84	80
Gender Female	59.3%	50.0%	54.2%
Gender Male	40.7%	50.0%	45.8%
Race: White	100%	83.3%	41.7%
Race: Asian	0%	16.7%	54.2%
Race: African American	0%	0%	4.2%

To ensure reliable clinical labeling, each patient’s ulcer outcome was determined by the vascular specialists based on a comprehensive clinical evaluation. This assessment integrated available ABI/TBI results, handheld Doppler findings, and direct wound inspection, consistent with real-world decision-making in vascular clinics. ABI/TBI indices were collected during the same visits as PA imaging whenever feasible; however, in patients with calcified or non-compressible arteries, these measurements were unreliable or unobtainable. In such cases, the physicians’ overall clinical judgment served as the final reference standard for defining healing, worsening, or stable outcomes.

The healthy volunteer group ($N = 24$) included 13 females (54.2%) and 11 males (45.8%). The racial composition was 13 identifying as Asian (54.2%), 10 as White (41.7%), and 1 as African American (4.2%). Their ages ranged from 22 to 80 years, with a mean of 43.5 ± 19.9 years. Each healthy participant was also imaged at least twice, with variable time intervals between sessions ranging from several weeks to over a year, to assess vascular reproducibility. This group included 10 young adults with no history of foot ulcers or peripheral vascular disease, and 14 individuals with prior ulcer history, but had either fully recovered or had the contralateral healthy foot imaged. These older volunteers were included to narrow the age gap with the patient cohort and to provide clinically stable, non-ischemic reference vasculature. All healthy participants had intact skin and no evidence of active ischemia at the time of imaging, minimizing confounding from remote ulcer history. A summary of the subject details can be found in Table 3.

Additional clinical information for the patient group included ulcer location, severity, surgical history, and Ankle–Brachial Index (ABI) or Toe–Brachial Index (TBI) measurements when available. This study was conducted in accordance with the ethical standards of the Declaration of Helsinki. The study protocol, including all imaging and data collection procedures, was approved by the University at Buffalo Institutional Review Board (University at Buffalo Institutional Review Board under protocol number STUDY00001165 and title “Photoacoustic and optical imaging of human foot”). Written informed consents were obtained from all participants.

Quantitative feature design and extraction

The ultimate goal of this study was to develop a robust supervised learning framework to classify foot ulcer status and monitor longitudinal vascular changes using quantitative photoacoustic features. To this end, we designed a comprehensive set of 45 quantitative features capturing signal, texture, and morphological information. These features were extracted from the reconstructed 3D PA volumes using a custom MATLAB pipeline and served as the basis for subsequent selection and modeling. Feature extraction was systematically performed in three spatial representations of each 3D photoacoustic volume: (1) the axial-lateral (XZ) plane, represented by a MAP image along the elevation (Y) direction; (2) the elevation-lateral (YZ) plane, represented by a MAP along the axial (X) direction; and (3) the full

volumetric 3D space. For brevity, features are labeled by the projection (collapsed) axis and view: “X” denotes features from the YZ MAP (projected along X; top view), “Y” denotes features from the XZ MAP (projected along Y; cross-section view), and “3D” denotes features from the full volumetric reconstruction.

Domain-specific ROIs were delineated on two orthogonal 2D MAPs and fused into a unified 3D ROI. Within this ROI, we use a two-level mask hierarchy: background vs. signal, with the signal further partitioned into vessel and tissue. The detailed visualization can be found in Fig. S1. For signal-region descriptors (e.g., SNR, entropy, gradient, skewness, kurtosis), ROI-restricted MAPs were intensity-thresholded and lightly dilated to capture boundary transitions; the same convention was applied in the X, Y, and 3D domains. For vessel/tissue–relative metrics (occupancy and compartment means/SDs), vessel masks were derived with a Frangi vesselness filter within the ROI in both X and Y. Skeletonization was applied only in X to compute vessel tortuosity (X), branch angle (X), and vessel density (X). By contrast, vessel diameter (Y) and vessel density (Y) were obtained from ROI-constrained segmentations without vesselness or skeletonization. All features were computed under this shared mask hierarchy and nomenclature to emphasize the vascular signal while limiting background leakage. Details can be found in Table 4.

The first category comprises signal- and intensity-based descriptors across the X (top view), Y (cross-sectional view), and 3D domains. PA Global Mean in the signal ROI summarizes the overall photoacoustic level and its variability, reflecting baseline vascular signal strength and heterogeneity. Vessel Mean and Tissue Mean in the vessel and tissue ROIs capture the contrast between vascular structures and surrounding tissue as well as intra-compartment variability, thus indexing the balance between perfused structures and parenchyma. On X/Y MAPs, 2D SNR contrasts the signal region with the local background; in 3D, SNR is the mean-to-variance ratio over non-zero voxels of the unified mask—together these provide complementary readouts of detectability and stability of vascular signal⁴⁷. Entropy in the signal region measures structural randomness and heterogeneity^{48,49}. Mean gradient indicates vessel-edge sharpness and

boundary definition. Skewness captures distributional asymmetry. Kurtosis captures tail weight and rare bright outliers. Metrics were computed on X/Y MAPs with boundary-inclusive signal ROIs and on the 3D volume^{50–52}.

The second category comprises texture-based descriptors across the X, Y, and 3D domains. Energy quantifies signal concentration. Homogeneity quantifies local gray-level uniformity. Fractal dimension captures multiscale structural complexity and space-filling behavior of vascular patterns. Together, these indices complement first-order measures by indicating whether the vascular signal is concentrated or diffuse, and regular or irregular across domains. Metrics were computed within the predefined X, Y, and 3D ROIs; when a signal region was required, boundary-inclusive signal masks were used^{53–57}.

The third category comprises morphology-based descriptors of geometry, caliber, and spatial coverage in different projections. In X projection (top view), vessel tortuosity, branch angle, and vessel density quantify path complexity, branching geometry, and network coverage^{58–65}. In the Y projection (cross-sectional view), vessel diameter and vessel density summarize apparent caliber and abundance. Across domains, vessel occupancy reports the fraction of the ROI labeled as vessel. In addition, vessel and tissue standard deviations summarize intra-compartment heterogeneity relevant to healing and ischemic change^{66,67}. Computation followed the mask hierarchy and domain rules defined above, applying a vesselness filter with skeletonization in X and ROI constrained segmentations in Y.

All features were computed within the predefined ROIs with identical settings across subjects and timepoints. Assigning metrics to X, Y, and 3D domains ensured anatomical relevance, and the three feature families jointly capture signal strength, spatial organization, and vascular geometry, enabling reproducible cross-sectional and longitudinal comparisons. Several of the first- and second-order descriptors (e.g., intensity moments, entropy, energy, homogeneity, and fractal dimension) follow standard formulations widely used in medical image analysis and radiomics^{68–71}. In this study, these established metrics were adapted to 3D photoacoustic vascular volumes and evaluated within PA-specific ROIs. They were further complemented by PA-driven vascular features (e.g., X/Y/3D vessel occupancy, vessel/tissue compartment statistics, and domain-specific tortuosity and gradient measures), which together form a unified, 45-dimensional feature panel tailored to longitudinal ulcer monitoring.

Table 4 | Categorization of 45 quantitative PA features by domain (X, Y, 3D)

First-order features/ signal-based	Second-order/texture- based features	Morphology/shape features
PA Global Mean (X)	Energy (X)	Vessel Tortuosity(X)
PA Global Mean (Y)	Energy (Y)	Branch Angle (X)
PA Global Mean (3D)	Energy (3D)	Vessel Diameter (Y)
PA Vessel Mean (X)	Homogeneity (X)	Vessel Density (X)
PA Vessel Mean (Y)	Homogeneity (Y)	Vessel Density (Y)
PA Tissue Mean (X)	Homogeneity (3D)	PA Global Std (X)
PA Tissue Mean (Y)	Fractal Dimension (X)	PA Global Std (Y)
SNR (X)	Fractal Dimension (Y)	PA Global Std (3D)
SNR (Y)	Fractal Dimension (3D)	PA Vessel Std (X)
SNR (3D)	Gradient Mean (X)	PA Vessel Std (Y)
Skewness (X)	Gradient Mean (Y)	PA Tissue Std (Y)
Skewness (Y)	Gradient Mean (3D)	PA Tissue Std (X)
Skewness (3D)		Vessel Occupancy (X)
Entropy (X)		Vessel Occupancy (Y)
Entropy (Y)		
Entropy (3D)		
Kurtosis (X)		
Kurtosis (Y)		
Kurtosis (3D)		

Feature selection

In this study, feature selection focused on quantifying changes in vascular characteristics over time. To achieve this, each subject was represented by a delta-based feature vector (Δ), computed as the difference between their two imaging sessions. This approach captured longitudinal changes within each subject relative to their own baseline. By doing so, it preserved physiologically meaningful dynamics that might be hidden in static, cross-sectional comparisons. All features were then standardized using z-score normalization to ensure comparability across subjects and metrics.

For each evaluation round, the dataset was split at the subject level using a random seed. Approximately 15% of patients in each clinical category (healing, worsening, and healthy) were held out for testing. All splits were based on unique patient identifiers to ensure that no subject appeared in both training and testing sets. This strict partitioning was essential to prevent data leakage and maintain independence between training and evaluation. All downstream procedures, including feature selection and model training, were confined strictly to the training set.

To identify discriminative features for each clinical outcome, we employed a one-vs-all LASSO regression strategy, training three separate models to distinguish each class from the rest. Each model was configured with an elastic-net mixing parameter ($\alpha = 0.5$), and the optimal penalty parameter (λ) was selected via 5-fold cross-validation within the training data. The three class-specific binomial LASSO models (healing, worsening, and healthy) produced sparse coefficient vectors (β) that captured class-specific contributions of each feature. These models were then aggregated to form a unified projection space that served as input for the downstream SVM classifier. This class-wise one-vs-rest formulation improved

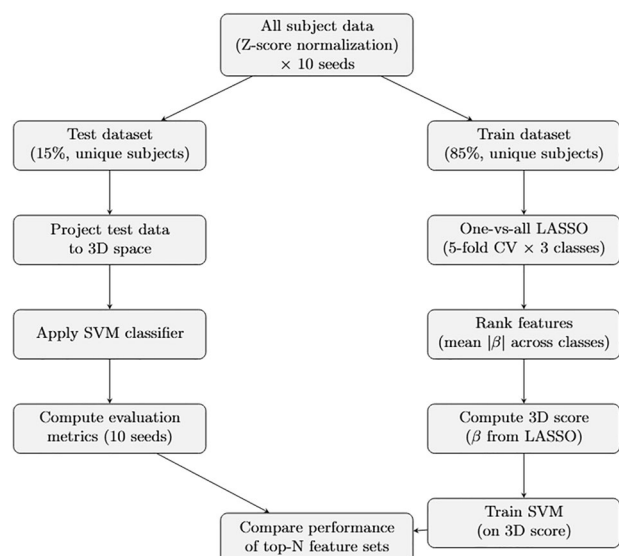


Fig. 10 | Schematic pipeline for multi-seed LASSO-based feature selection, 3D projection, and SVM classification with hold-out testing.

interpretability and robustness to class imbalance, rather than using a single multinomial LASSO approach. To evaluate the stability and interpretability of selected features, we averaged the absolute β coefficients across 10 independent train-test splits. Features were ranked based on these aggregated importance scores, and four subsets—Top-6, Top-12, Top-24, and Top-45—were derived. These subset sizes were not chosen to define an optimal model. Instead, they span a range of feature sparsity levels, allowing us to examine how classification performance and biological interpretability change with model complexity. Notably, the Top-45 subset included all candidate features and served as a comparative baseline for downstream analysis, offering a reference point for trade-offs between performance and overfitting risk in small datasets. Finally, each subject's delta vector was projected onto the three class-specific β vectors obtained from the training set. This projection produced a compact, three-dimensional class score vector that served as the low-dimensional input to the outcome classifier. The overall procedure is summarized in Fig. 10.

Model validation

The classification model was evaluated on the 15% of testing subjects held out during each data split, following the same subject-level partitioning strategy described above. These test subjects were excluded from all feature selection and model training procedures, ensuring a strictly independent evaluation set. Each subject's delta-based (Δ) feature vector was first projected onto the LASSO-derived coefficient vectors obtained from the corresponding training set, producing a three-dimensional class score representation. These compact and interpretable vectors served as input features to the downstream classification model.

For each evaluation round, a multi-class support vector machine (SVM) was trained on the training-set-derived class score vectors. The classifier was implemented using a radial basis function (RBF) kernel within an error-correcting output code (ECOC) framework to support three-way classification among healing, worsening, and healthy groups. The SVM hyperparameters (C and γ) were tuned within each training fold using a grid search with five-fold cross-validation on the training data only. The best-performing parameter combination was then applied to the corresponding held-out test subjects, ensuring complete separation between training and evaluation. The LASSO coefficients used for projection were fixed from the training phase and applied without modification to the test subjects, preventing any information leakage. To ensure robust and unbiased performance estimates, the entire modeling pipeline—including data splitting, LASSO projection, and SVM training—was repeated across ten independent

random seeds, each defining a unique train-test split. Rather than seeking a single “optimal” model, we adopted this multi-seed approach to mitigate sampling variability and assess the stability of classification behavior across different training subsets. For each seed and each feature subset (Top-6, Top-12, Top-24, Top-45), a full cycle of training and evaluation was conducted. Model predictions, class probabilities, confusion matrices, and other outputs were recorded to enable downstream quantitative analysis.

Model performance was evaluated using three primary metrics: overall accuracy, macro-averaged area under the ROC curve (AUC), and per-class recall for healing, worsening, and healthy outcomes. Confusion matrices were averaged across seeds to visualize class-wise consistency and misclassification patterns. Performance metrics from all seeds were then aggregated for each Top- N configuration. These results enabled comparative evaluation across feature sparsity levels, highlighting the trade-offs between model complexity and classification robustness. This multi-seed comparative analysis summarized model accuracy, macro AUC, and per-class recall, while illustrating how varying feature sparsity levels affected classification robustness. In addition, the analysis highlighted the contribution of specific vascular features to longitudinal ulcer outcome stratification. Because the study cohort was of modest size and performance was summarized across 10 random train-test splits, we additionally quantified the uncertainty and robustness of the Top-12 configuration. All hold-out predictions from the ten splits were pooled, and overall test accuracy and macro-averaged AUC were computed on this aggregated set. To obtain 95% confidence intervals for these pooled metrics, we applied non-parametric bootstrap resampling of the pooled test subjects (10,000 iterations). In parallel, a label permutation test (5000 iterations) was performed by randomly shuffling the pooled test labels, recomputing accuracy and macro AUC for each permuted dataset. The resulting null distributions were used to derive permutation p -values for the observed performance, which are reported in the Results.

Data availability

The data that support the findings of this study are available from the corresponding author upon reasonable request.

Code availability

The MATLAB scripts used for ROI extraction, quantitative feature computation, and classification are publicly available in the Zenodo repository at <https://doi.org/10.5281/zenodo.17992387>.

Received: 4 September 2025; Accepted: 27 January 2026;

Published online: 27 February 2026

References

- Conte, M. S. et al. Global vascular guidelines on the management of chronic limb-threatening ischemia. *Eur. J. Vasc. Endovasc. Surg.* **58**, S1–S109.e133 (2019).
- Shan, L. L. et al. Quality of life in chronic limb threatening ischaemia: systematic review and meta-analysis. *Eur. J. Vasc. Endovasc. Surg.* **64**, 666–683 (2022).
- Tan, P., Lim, J. & Moiemien, N. Imaging techniques used for wound healing assessment: a systematic review part 1 chronic wounds. *Eur. Burn J.* **2**, 194–214 (2021).
- Monroy, B. et al. Automated chronic wounds medical assessment and tracking framework based on deep learning. *Comput. Biol. Med.* **165**, 107335 (2023).
- Soyoye, D. O. et al. Diabetes and peripheral artery disease: a review. *World J. Diabetes* **12**, 827–838 (2021).
- Marso, S. P. & Hiatt, W. R. Peripheral arterial disease in patients with diabetes. *J. Am. Coll. Cardiol.* **47**, 921–929 (2006).
- Chao, C. Y. & Cheing, G. L. Microvascular dysfunction in diabetic foot disease and ulceration. *Diabetes Metab. Res. Rev.* **25**, 604–614 (2009).
- Manu, C. A. et al. Peripheral arterial disease located in the feet of patients with diabetes and foot ulceration demands a new approach

- to the assessment of ischemia. *Int. J. Low. Extrem. Wounds* **21**, 397–404 (2022).
9. Zubair, M., Al Amri, M. & Ahmad, J. A retrospective study of ABI and TBI during the healing of ulcer among diabetic patients. *Diabetes Metab. Syndr.* **13**, 78–83 (2019).
 10. AbuRahma, A. F. et al. Critical analysis and limitations of resting ankle-brachial index in the diagnosis of symptomatic peripheral arterial disease patients and the role of diabetes mellitus and chronic kidney disease. *J Vasc Surg* **71**, 937–945 (2020).
 11. Suludere, M. A. et al. Near-infrared spectroscopy data for foot skin oxygen saturation in healthy subjects. *Int. Wound J.* **21**, e14814 (2024).
 12. Arnold, J. & Marmolejo, V. L. Interpretation of near-infrared imaging in acute and chronic wound Care. *Diagnostics* **11**, 778 (2021).
 13. Dinh, M. T., Abad, C. L. & Safdar, N. Diagnostic accuracy of the physical examination and imaging tests for osteomyelitis underlying diabetic foot ulcers: meta-analysis. *Clin. Infect. Dis.* **47**, 519–527 (2008).
 14. Kapoor, A. et al. Magnetic resonance imaging for diagnosing foot osteomyelitis: a meta-analysis. *Arch. Intern. Med.* **167**, 125–132 (2007).
 15. Sibley, R. C. et al. Noninvasive Physiological Vascular Studies: A Guide to Diagnosing Peripheral Arterial Disease. *RadioGraphics* **37**, 346–357 (2017).
 16. Petri, M. et al. Photoacoustic imaging of real-time oxygen changes in chronic leg ulcers after topical application of a haemoglobin spray: a pilot study. *J. Wound Care* **25**, 87–91 (2016).
 17. Li, S. et al. Photoacoustic imaging of peripheral vessels in extremities by large-scale synthetic matrix array. *J. Biomed. Opt.* **29**, S11519–S11519 (2024).
 18. Ahmad, M., Patel, K., Davies, A. H. & Shalhoub, J. Noninvasive optical methods to assess tissue perfusion in patients with peripheral arterial disease and diabetes mellitus: a scoping review and discussion. *JVS-Vasc. Insights* **2**, 100034 (2024).
 19. Cleofort, V. et al. Evaluation of the ankle brachial index and toe brachial index for peripheral arterial disease diagnosis in patients over 70 years with lower limb ulcers. *JMV-J. Méd. Vasc.* **48**, 11–17 (2023).
 20. Rizki, M. N., Suhartono, R. & Herqutanto, H. Comparison of ABI, TBI, TOE pressure, and ankle pressure examinations in pad patients, before and after angioplasty with and without type 2 DM at RSCM. *J. Locus Penelit. dan Pengabd.* **4**, 8267–8278 (2025).
 21. Wang, L. *Photoacoustic Imaging and Spectroscopy*. (CRC Press, 2017).
 22. Zhang, H. et al. OneTouch automated photoacoustic and ultrasound imaging of breast in standing pose. *IEEE Trans. Med. Imaging PP* **44**, 4617–4626 (2025).
 23. Mantri, Y. et al. Photoacoustic monitoring of angiogenesis predicts response to therapy in healing wounds. *Wound Repair Regen* **30**, 258–267 (2022).
 24. Mezrich, R. S. Shine a light: listen to the echo of disease—using photoacoustic imaging to evaluate diabetic foot and wound healing. *Radiology* **303**, 474–475 (2022).
 25. Harii, A., Chen, F., Moore, C. & Jokerst, J. V. Noninvasive staging of pressure ulcers using photoacoustic imaging. *Wound Repair Regen* **27**, 488–496 (2019).
 26. Mantri, Y. & Jokerst, J. V. Impact of skin tone on photoacoustic oximetry and tools to minimize bias. *Biomed. Opt. Express* **13**, 875–887 (2022).
 27. Park, J. et al. Clinical translation of photoacoustic imaging. *Nat. Rev. Bioeng.* **3**, 193–212 (2025).
 28. Kuniyil Ajith Singh, M., Sato, N., Ichihashi, F. & Sankai, Y. Clinical translation of photoacoustic imaging—opportunities and challenges from an industry perspective. In *LED-Based Photoacoustic Imaging: From Bench to Bedside* (ed. Kuniyil Ajith Singh, M.) 379–393 https://doi.org/10.1007/978-981-15-3984-8_16 (Springer, Singapore, 2020).
 29. Armstrong, A. K. et al. Feasibility of MRI-guided cardiac catheterization, angioplasty, and stenting in a commercial wide-bore 0.55 T scanner. *J. Cardiovasc. Magn. Reson.* **27**, 101858 (2025).
 30. Tardaguila-Garcia, A. et al. Could X-ray predict long-term complications in patients with diabetic foot osteomyelitis? *Adv. Skin Wound Care* **35**, 1–5 (2022).
 31. Yao, J. & Wang, L. V. Photoacoustic microscopy. *Laser Photonics Rev.* **7**, 758–778 (2013).
 32. Huang, C. et al. Dual-scan photoacoustic tomography for the imaging of vascular structure on foot. *IEEE Trans Ultrason Ferroelectr Freq Control* **70**, 1703–1713 (2023).
 33. Davnall, F. et al. Assessment of tumor heterogeneity: an emerging imaging tool for clinical practice? *Insights Imaging* **3**, 573–589 (2012).
 34. Kim, H. Y. et al. Comparison of CT- and MRI-based quantification of tumor heterogeneity and vascularity for correlations with prognostic biomarkers and survival outcomes: a single-center prospective cohort study. *Bioengineering* **10**, 504 (2023).
 35. Tonnesen, M. G., Feng, X. & Clark, R. A. Angiogenesis in wound healing. *J. Investig. Dermatol. Symp. Proc.* **5**, 40–46 (2000).
 36. Diestro, J. D. B. et al. Perfusion vs non-perfusion computed tomography imaging in the late window of emergent large vessel ischemic stroke: a systematic review and meta-analysis. *PLoS ONE* **19**, e0294127 (2024).
 37. Hopkins, S. R. et al. Abnormal pulmonary perfusion heterogeneity in patients with Fontan circulation and pulmonary arterial hypertension. *J. Physiol.* **599**, 343–356 (2021).
 38. Bagher-Ebadian, H. et al. Radiomics characterization of tissues in an animal brain tumor model imaged using dynamic contrast enhanced (DCE) MRI. *Sci. Rep.* **13**, 10693 (2023).
 39. El Kaffas, A. et al. Spatial characterization of tumor perfusion properties from 3D DCE-US perfusion maps are early predictors of cancer treatment response. *Sci. Rep.* **10**, 6996 (2020).
 40. Hofmann, B. B. et al. Evaluation of MTT heterogeneity of perfusion CT imaging in the early brain injury phase: an insight into asah pathophysiology. *Brain Sci.* **13**, 824 (2023).
 41. Chimura, M. et al. Novel indices representing heterogeneous distributions of myocardial perfusion imaging. *Ann. Nucl. Med.* **38**, 468–474 (2024).
 42. Urano, M. et al. Quantitative evaluation of lower limb varicose veins using photoacoustic imaging. *J. Med. Ultrason.* **51**, 507–516 (2024).
 43. Miao, X. et al. Dynamic characterization of vascular response and treatment in oral traumatic ulcer in mice via photoacoustic imaging. *Quant Imaging Med. Surg.* **14**, 4333–4347 (2024).
 44. Knieling, F., Lee, S. & Ntziachristos, V. A primer on current status and future opportunities of clinical optoacoustic imaging. *Npj Imaging* **3**, 4 (2025).
 45. Attia, A. B. E. et al. A review of clinical photoacoustic imaging: current and future trends. *Photoacoustics* **16**, 100144 (2019).
 46. Grohl, J., Schellenberg, M., Dreher, K. & Maier-Hein, L. Deep learning for biomedical photoacoustic imaging: a review. *Photoacoustics* **22**, 100241 (2021).
 47. Cosman, P. C., Gray, R. M. & Olshen, R. A. Evaluating quality of compressed medical images—snr, subjective rating, and diagnostic-accuracy. *Proc. IEEE* **82**, 919–932 (1994).
 48. Yadav, P. S., Gupta, B. & Lamba, S. S. A new approach of contrast enhancement for medical images based on entropy curve. *Biomed. Signal Process. Control* **88**, 105625 (2024).
 49. Raja, N. S. M. et al. Contrast enhanced medical MRI evaluation using Tsallis entropy and region growing segmentation. *J. AmbientIntell. Humani. Comput.* **15**, 961–972 <https://doi.org/10.1007/s12652-018-0854-8> (2024).
 50. Chiamaka Okafor, N. et al. The effect of image preprocessing algorithms on diabetic foot ulcer classification. In *Annual Conference on Medical Image Understanding and Analysis, Lecture Notes in Computer Science* 14860, 336–352 (Springer, 2024).

51. Niri, R., Lucas, Y., Treuillet, S. & Douzi, H. Smartphone-based thermal imaging system for diabetic foot ulcer assessment. In Journées d'Etude sur la TéléSanté (JETSAN) (Sorbonne Université, Paris, France, 23–24 May 2019). HAL: hal-02161044.
52. Mahamudul Hasan, M., Yap, M. H. & Kamrul Hasan, M. Venn Diagram Multi-label Class Interpretation of Diabetic Foot Ulcer with Color and Sharpness Enhancement. Preprint at <https://doi.org/10.48550/arXiv.2305.01044> (2023).
53. Patwari, M. et al. A quantitative comparison of plantar soft tissue strainability distribution and homogeneity between ulcerated and non-ulcerated patients using ultrasound strain elastography. *Proc. Inst. Mech. Eng. H* **236**, 722–729 (2022).
54. Duan, Y. et al. Texture differences of microchambers and macrochambers in heel pads between the elderly with and without diabetes. *J Tissue Viability* **33**, 584–590 (2024).
55. Wang, L. et al. Area Determination of Diabetic Foot Ulcer Images Using a Cascaded Two-Stage SVM-Based Classification. *IEEE Trans. Biomed. Eng.* **64**, 2098–2109 (2017).
56. Jones, T. D. & Plassmann, P. An active contour model for measuring the area of leg ulcers. *IEEE Transactions on Medical Imaging* **19**, 1202–1210 (2000).
57. Rani, P., Aliahmad, B. & Kumar, D. K. A novel approach for quantification of contour irregularities of diabetic foot ulcers and its association with ischemic heart disease. In 2017 39th annual international conference of the IEEE Engineering in Medicine and Biology Society (EMBC), 1437–1440 (IEEE, 2017).
58. Lee, H., Lee, M., Chung, H. & Kim, H. C. Quantification of retinal vessel tortuosity in diabetic retinopathy using optical coherence tomography angiography. *Retina* **38**, 976–985 (2018).
59. Wang, S. H. et al. An overview of clinical examinations in the evaluation and assessment of arterial and venous insufficiency wounds. *Diagnostics* **13**, 2494 (2023).
60. Untracht, G. R. et al. Pilot study of optical coherence tomography angiography-derived microvascular metrics in hands and feet of healthy and diabetic people. *Sci Rep.* **13**, 1122 (2023).
61. Iroshan, K. et al. Detection of diabetes by macrovascular tortuosity of superior bulbar conjunctiva. In 2018 40th Annual International Conference of the IEEE Engineering in Medicine and Biology Society (EMBC), 1–4 (IEEE, 2018).
62. Chomel, S. et al. Contrast-enhanced MR angiography of the foot: anatomy and clinical application in patients with diabetes. *AJR Am. J. Roentgenol.* **182**, 1435–1442 (2004).
63. Ding, J. et al. Early retinal arteriolar changes and peripheral neuropathy in diabetes. *Diabetes Care* **35**, 1098–1104 (2012).
64. Mani, R., Holmes, J., Rerkasem, K. & Papanas, N. Blood vessel density measured using dynamic optical coherence tomography is a tool for wound healers. *Int. J. Low. Extrem. Wounds* **22**, 235–240 (2023).
65. Moura, L. I., Dias, A. M., Carvalho, E. & de Sousa, H. C. Recent advances on the development of wound dressings for diabetic foot ulcer treatment—a review. *Acta Biomater* **9**, 7093–7114 (2013).
66. Li, J. et al. Investigating the healing mechanisms of an angiogenesis-promoting topical treatment for diabetic wounds using multimodal microscopy. *J Biophotonics* **11**, e201700195 (2018).
67. Nayak, C. & Kaur, L. Retinal blood vessel segmentation for diabetic retinopathy using multilayered thresholding. *Int. J. Sci. Res.* **4**, 1520–1526 (2015).
68. Haralick, R. M., Shanmugam, K. & Dinstein, I. H. Textural features for image classification. *IEEE Trans. Syst. Man Cybern.* SMC-3, 610–621 <https://doi.org/10.1109/TSMC.1973.4309314> (1973).
69. Aerts, H. J. et al. Decoding tumour phenotype by noninvasive imaging using a quantitative radiomics approach. *Nat. Commun.* **5**, 4006 (2014).
70. Zwanenburg, A. et al. The image biomarker standardization initiative: standardized quantitative radiomics for high-throughput image-based phenotyping. *Radiology* **295**, 328–338 (2020).
71. Kumar, V. et al. Radiomics: the process and the challenges. *Magn. Reson. Imaging* **30**, 1234–1248 (2012).

Acknowledgements

This work was supported in part by the National Institutes of Health under grant numbers R01EB029596, R01EB028978, and R01EB035188.

Author contributions

Y.C. contributed to study design, data analysis, implementation, and manuscript writing. C.H. collected data and assisted with implementation. S.-I.Y. performed statistical analysis and contributed to methodology. S.C. provided statistical design and supervision. Y.X. was responsible for visualization and data presentation. R.W.B. developed the hardware system. H.Z. contributed to system design. I.K. assisted with patient recruitment. L.M.H. provided clinical supervision. W.X. contributed technical supervision. J.X. supervised the overall study and revised the manuscript. All authors read and approved the final manuscript.

Competing interests

The authors declare no competing interests.

Additional information

Supplementary information The online version contains supplementary material available at <https://doi.org/10.1038/s44303-026-00143-0>.

Correspondence and requests for materials should be addressed to Jun Xia.

Reprints and permissions information is available at <http://www.nature.com/reprints>

Publisher's note Springer Nature remains neutral with regard to jurisdictional claims in published maps and institutional affiliations.

Open Access This article is licensed under a Creative Commons Attribution-NonCommercial-NoDerivatives 4.0 International License, which permits any non-commercial use, sharing, distribution and reproduction in any medium or format, as long as you give appropriate credit to the original author(s) and the source, provide a link to the Creative Commons licence, and indicate if you modified the licensed material. You do not have permission under this licence to share adapted material derived from this article or parts of it. The images or other third party material in this article are included in the article's Creative Commons licence, unless indicated otherwise in a credit line to the material. If material is not included in the article's Creative Commons licence and your intended use is not permitted by statutory regulation or exceeds the permitted use, you will need to obtain permission directly from the copyright holder. To view a copy of this licence, visit <http://creativecommons.org/licenses/by-nc-nd/4.0/>.

© The Author(s) 2026